# FULL PAPER

**Sensors**

ADVANCED
FUNCTIONAL
MATERIALS

www.afm-journal.de

# Complementary Electromagnetic-Triboelectric Active Sensor for Detecting Multiple Mechanical Triggering

*Peihong Wang, Ruiyuan Liu, Wenbo Ding, Peng Zhang, Lun Pan, Guozhang Dai, Haiyang Zou, Kai Dong, Cheng Xu, and Zhong Lin Wang\**

With the fast development of integrated circuit technology and internet of things, sensors with multifunctional characteristics are desperately needed. This work presents an integrated electromagnetic-triboelectric active sensor (ETAS) for simultaneous detection of multiple mechanical triggering signals. The good combination of a contact-separation mode triboelectric nanogenerator (TENG) and an electromagnetic generator (EMG) realizes the complement of their individual advantages. The theoretical calculation and analysis of EMG and TENG are performed to understand the relationship between their output and the external mechanical signals. The experimental results show that the output voltage of TENG part is suitable to detect the magnitude of the external triggering force with a sensitivity of about 2.01 V N$^{-1}$. Meanwhile, the output current of EMG part is more appropriate to reflect the triggering velocity and the sensitivity is about 4.3 mA (m s$^{-1}$)$^{-1}$. Moreover, both the TENG part and the EMG part exhibit good stabilities after more than 20 000 cycles of force loading and unloading. One ETAS that can record the typing behavior of the finger precisely is demonstrated. In addition, the TENG part can harvest the mechanical energy during typing for possible powering of tiny electronics. This ETAS has promising applications in complex human–machine interface, personal identification, and security system.
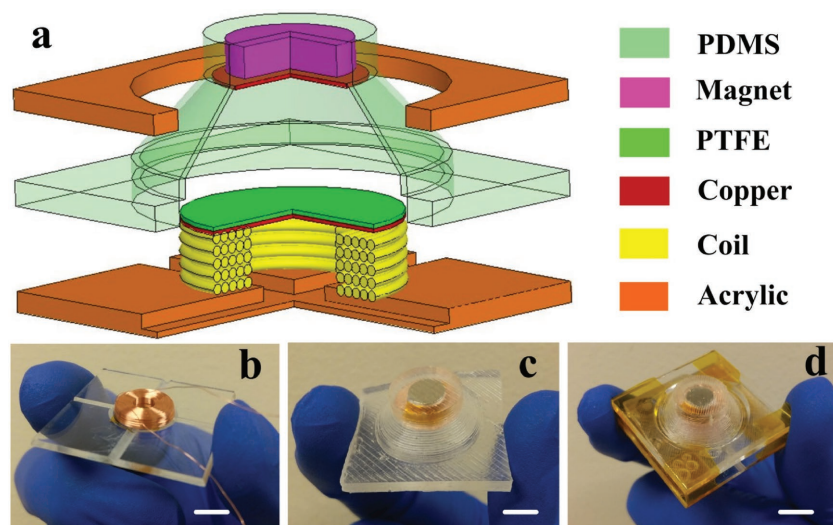
## 1. Introduction

With the fast development of wireless sensor networks and internet of things, the demands on the properties of various sensors are increasing.[1–3] Sensors with the characteristics of fast response, high integration, multifunction, and self-powered ability are preferred.[4] Recently, triboelectric nanogenerators (TENGs), which are based on the coupling of triboelectrification and electrostatic induction, have been proven as an effective method to convert almost all forms of mechanical energy into electric power.[5–11] Meanwhile, TENGs can also be used as self-powered sensors to actively detect pressure, vibration, sounds, tactile, magnetic fields, gesture, and so on.[12–19] However, the TENGs suffer from a low-output current with a relatively high-output voltage in comparison with the electromagnetic generators (EMGs). Based on Faraday's electromagnetic induction law, EMG can convert much mechanical energy into electricity and has a relatively high-output current but low-output voltage. Similar with TENGs, EMGs also have two main functions of energy harvesting and self-powered sensing.[20,21] However, the signals that EMG and TENG can efficiently detect are different due to their different sensing mechanisms, namely the TENG has a better performance at low frequency (typically 0.1–3 Hz) while EMG has good output at high frequency (>5 Hz).[22] As an energy harvesting method, many hybridized electromagnetic-TENGs have been developed to harvest biomechanical energy, blue energy, wind energy, vibration energy, and more, by using the advantage of their each part.[23–28] Nevertheless, combining EMG and TENG together for multisignal detections has not been reported yet.

Here in this work, we demonstrate a robust and function-complementary electromagnetic-triboelectric active sensor (ETAS) for simultaneously detecting the force and velocity of mechanical triggering. By integrating one contact-separation mode TENG and one EMG together, the device can generate two signals at the same time. The output voltage of TENG part can detect static signals such as force/pressure; meanwhile, the output current of EMG part can monitor dynamic signal, such as motion velocity. The theoretical and experimental results indicate that the ETAS could achieve a good complementarity of sensing function of EMG and TENG. Furthermore, the demonstration shows that the hybridized active sensor can precisely record the typing behavior of typist, such as pressing force, typing velocity, and typing frequency. Therefore, this work will open a new field for application of electromagnetic-triboelectric

Dr. P. Wang, R. Liu, Dr. W. Ding, P. Zhang, Dr. L. Pan, Dr. G. Dai, H. Zou, K. Dong, Dr. C. Xu, Prof. Z. L. Wang
School of Materials Science and Engineering
Georgia Institute of Technology
Atlanta, GA 30332-0245, USA
E-mail: zhong.wang@mse.gatech.edu
Dr. P. Wang
School of Physics and Materials Science
Anhui Univeristy
Hefei, Anhui 230601, China
Prof. Z. L. Wang
Beijing Institute of Nanoenergy and Nanosystems
Chinese Academy of Sciences
Beijing 100083, China

ADVANCED
SCIENCE NEWS
www.advancedsciencenews.com

ADVANCED
FUNCTIONAL
MATERIALS
www.afm-journal.de

**Figure 1.** Structure design of the hybridized EMG-TENG active sensor. a) Schematic illustration of the multilayer structure of the hybridized sensor. b) The optical photograph of the Cu coil on the acrylic substrate (scale bar: 5 mm). c) The optical photograph of the PDMS button structure (scale bar: 5 mm). d) The optical photograph of the assembled hybridized sensor with a volume of about 25 × 25 × 13 mm³ (scale bar: 5 mm).

active sensors in touch sensing, human–machine interface, security system, and flexible electronics.
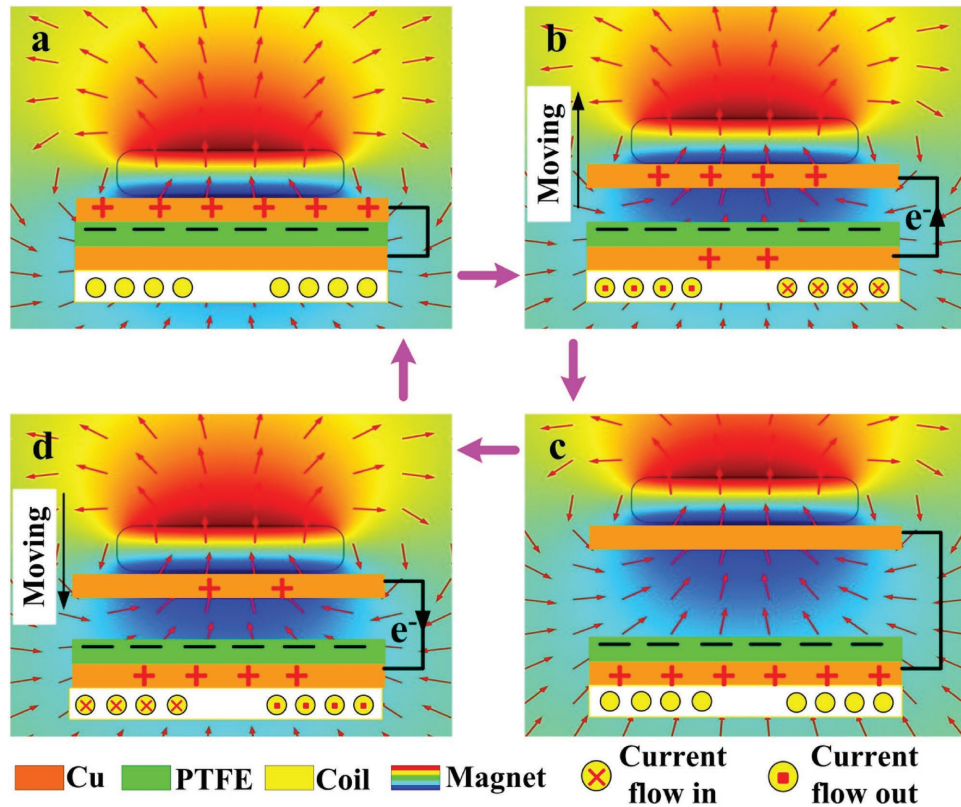
## 2. Results and Discussion

### 2.1. Device Structure

This hybridized active sensor has a multilayered structure as schematically illustrated in **Figure 1**a. A piece of acrylic sheet with dimension of 25 × 25 × 1.6 mm³ was prepared by laser cutting as a substrate. Four grooves are fabricated on the top of the substrate to prevent air from being sealed inside the structure. A copper (Cu) coil with turns of 600 was fixed on the center of the substrate as shown in Figure 1b. The inner resistance of the coil is 34 Ω. One layer of Cu foil was attached onto the coil as the bottom electrode of the TENG part. Then a 500 µm polytetrafluoroethylene (PTFE) film was attached onto the bottom electrode as the triboelectric material. A button structure as shown in Figure 1c is the key part of the hybridized sensor. The key-like structure is made of polydimethylsiloxane (PDMS) and its detailed fabrication process is given in Figure S1 in the Supporting Information. The trapezoidal structure of the PDMS button is more helpful to the uniform release of the force than the rectangular structure reported previously.[29] An NdFeB permanent magnet with a diameter of 6 mm and a height of 1.5 mm was sealed in the PDMS button structure and was used to generate the magnetic field for the coil. The weight of the magnet is 0.39 g. Another piece of acrylic sheet substrate was used to fix the PDMS button structure on the top. An assembled hybridized sensor with a volume of about 25 × 25 × 13 mm³ is shown in Figure 1d. Other fabrication information is in Experimental Section.

### 2.2. Working Principle

The working principle of the hybridized sensor includes two parts: the triboelectric part and the electromagnetic part, as illustrated in **Figure 2**. The working operation of the TENG part is based on contact triboelectrification and electrostatic induction, of which the fundamental physics can be attributed to Maxwell's displacement current.[30] As shown in Figure 2a, there is a full contact between the top Cu electrode and the PTFE film when the magnet moves to the lowest position. Equal amount of negative and positive charges appear on the contacted surfaces, respectively, due to the different triboelectricity between Cu and PTFE. Since Cu is more triboelectrically positive than PTFE, electrons are injected from Cu electrode into the surface of PTFE film.[31] As a result, positive charges are accumulated on the Cu side and the negative charges are accumulated on the PTFE side. The magnet will then move up due to the elastic force of the PDMS button structure when the external force is withdrawn. As a result, there is an electric potential difference (EPD) between the two electrodes and the EPD drives electrons to flow from the bottom electrode to the top electrode. Thus, the current is generated in the external circuit as shown in Figure 2b. The negative charge transfer from the bottom electrode to the top electrode continues in the whole process of magnet's releasing until the magnet arrives at its highest position. Therefore, no current can flow in the external circuit when the magnet is motionless as shown in Figure 2c. Subsequently, the magnet will move downward under the external force and then the EPD drives electrons flow from the top electrode to the bottom electrode and thus the current is generated as shown in Figure 2d. When the top electrode contacts with the PTFE film again, the current disappeared and one working cycle of the TENG is finished.

On the other hand, the EMG is based on Faraday's electromagnetic induction effect. As shown in Figure 2b, when the magnet moves upward, the magnetic flux that crosses the coil decreases and so the induced current is generated in the coil to compensate the decrease of the magnetic flux in the coil. When the magnet stops moving as shown in Figure 2c, the magnetic flux in the coil keep constant so that the inductive electromotive force in the coil is equal to zero. Therefore, no current flows in the coil. When the external force drives the magnet to move downward as shown in Figure 2d, the magnetic flux that crosses the coil increases and so the induced current is generated in the coil to offset the increase of the magnetic flux in the coil. Because the changing trend of the magnetic flux in the coil in Figure 2b,d are opposite, the direction of the induced current is also opposite as shown in Figure 2b,d. When the magnet arrives to its lowest position and has no movement as shown in Figure 2a, the magnetic flux in the coil has no change and then the induced current is zero. After that, a new cycle starts. Therefore, this hybridized nanogenerator can simultaneously produce two different electrical signals from EMG and TENG.

ADVANCED
SCIENCE NEWS

www.advancedsciencenews.com

ADVANCED
FUNCTIONAL
MATERIALS

www.afm-journal.de

**Figure 2.** Schematic of the operation principle of the hybridized sensor. When the magnet is moved up and down by external force, both the TENG and EMG can generate the output voltage and current signals. A 2D axisymmetric model of the magnet was established, and the distribution of the magnetic scalar potential and the magnetic flux density were calculated by COMSOL and shown by different color and red arrows, respectively.

The signals will be used to detect different physical signals in the following parts.

### 2.3. Theoretical Analysis of EMG

For a cylinder magnet as shown in Figure S2 (Supporting Information), the magnetic flux density $B$ at a distance $z$ from the center of the magnet surface can be calculated by the following equation[32]

$$B(z) = \frac{B_r}{2}\left(\frac{z+d}{\sqrt{(z+d)^2+R^2}} - \frac{z}{\sqrt{z^2+R^2}}\right) \quad (1)$$

where $B_r$ is the remanence of the magnet, $z$ is the distance of the point from the center of the magnet, and $R$ and $d$ are the radius and the thickness of the magnet, respectively.

According to Faraday's induction law, the electromotiveforce ($V_{emf}$) induced in a coil is proportional to time-rate change of magnetic flux linkage through a coil and is given as following

$$V_{emf} = -N\frac{d\Phi}{dt} \quad (2)$$

where $\Phi$ is the total magnetic flux linkage in one turn of the coil and $N$ is the number of the coil's turns. For an EMG system

which consists of a stationary coil and a movable magnet as shown in **Figure 3**a, the $V_{emf}$ in the coil can be expressed as
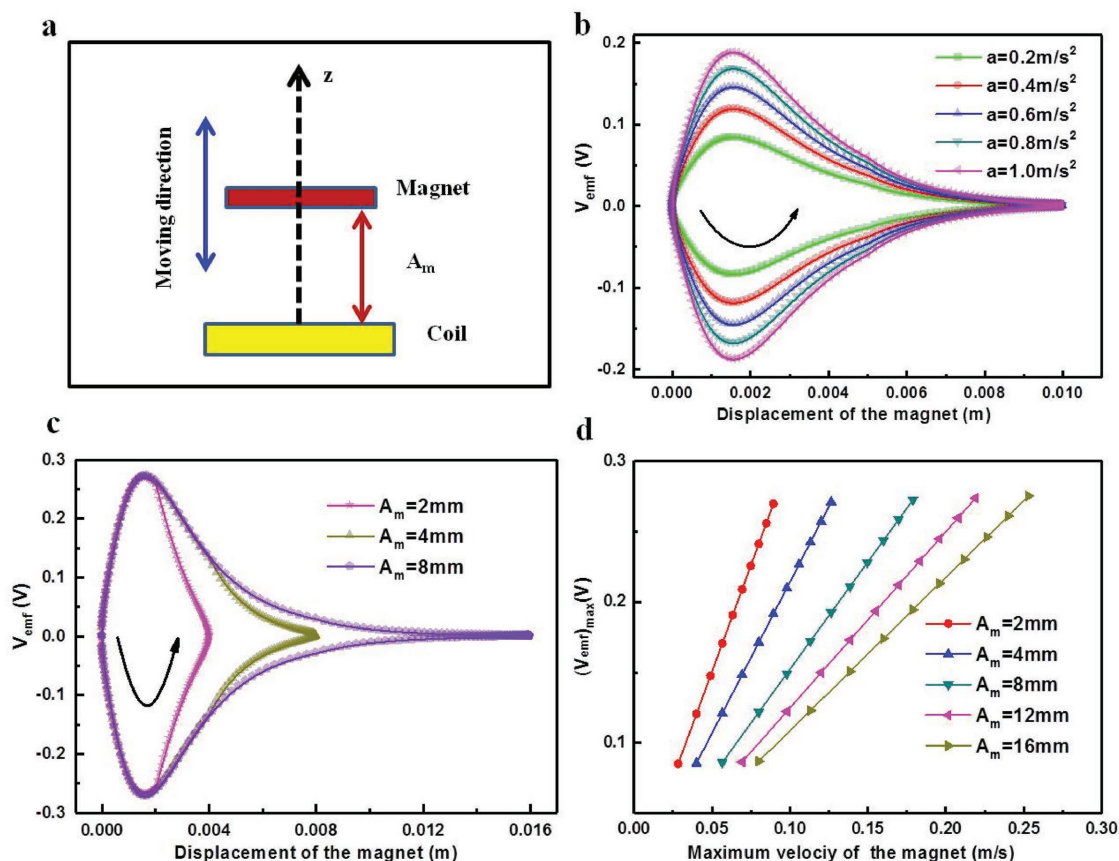
$$V_{emf} = -N\frac{d\Phi}{dt} = -N\frac{d(BS)}{dt} = -NS\frac{d(B(z))}{dz}\frac{dz}{dt} = -NS\frac{d(B(z))}{dz}v \quad (3)$$

where $B$ is the magnetic flux density through the coil, $S$ is the area of the coil, $z$ is the displacement of the magnet, and $v$ is the velocity of the magnet. Because the magnet is movable, the magnetic flux density ($B$) through the coil is changeable and depends on the position of the magnet. If the coil is connected into an electrometer directly, the short circuit current ($I_{sc}$) generated in the coil should be expressed as

$$I_{sc} = \frac{V_{emf}}{R_{coil}} = -\frac{NS}{R_{coil}}\frac{d(B(z))}{dz}v \quad (4)$$

where $R_{coil}$ is the internal resistance of the coil. Equations (3) and (4) mean that the open circuit voltage and the short-circuit current are proportional to $dB/dz$ and the velocity of the magnet.

According to the Equations (1), (3), and (4), the value of $V_{emf}$ and $I_{sc}$ can be calculated if the velocity of the magnet, the function of $B(z)$ and the parameters of the coil are known. In the following calculation, the dimension of the magnet is the same with that as mentioned in previous part 2.1, the diameter of the

ADVANCED
SCIENCE NEWS
www.advancedsciencenews.com

ADVANCED
FUNCTIONAL
MATERIALS
www.afm-journal.de

**Figure 3.** Theoretical calculation results of EMG. a) The schematic of magnet's movement ($A_m$ means the amplitude of the magnet). b) The value of $V_{emf}$ versus the displacement and the acceleration of the magnet when $A_m = 5$ mm. c) The value of $V_{emf}$ versus the displacement and the amplitude of the magnet when $a = 2$ m s$^{-2}$. d) The maximum value of $V_{emf}$ versus the maximum velocity and the amplitude of the magnet.

coil is fixed at 11 mm, and the coil has 600 turns. Moreover, it is assumed that the motion behavior of the magnet is known. Then the dependence of $V_{emf}$ on the displacement, amplitude, and acceleration of the magnet can be calculated and the calculated $V_{emf}$ versus different parameters in one cycle of magnet's movement are shown in Figure 3b,c. For example, when the amplitude and the acceleration/deceleration of the magnet is 5 mm and 1 m s$^{-2}$, respectively, the value of $v$, $B$, d$B$/d$z$, and $V_{emf}$ versus time and the displacement of the magnet are given in Figures S3 and S4 (Supporting Information). Here, the goal that we use constant amplitude and acceleration is that it is convenient to calculate the velocity of the loading.

Figure 3b indicates that the absolute value of $V_{emf}$ increased first and then decreased as the magnet moved away from or toward the coil when the acceleration ($a$) of the magnet was fixed. Meanwhile, the absolute value of $V_{emf}$ increased with the increasing acceleration of the magnet. However, the position of the magnet corresponding to the maximum value of $V_{emf}$ is unchangeable and is independent of the acceleration of the magnet. It can be seen from Figure 3b that the distance between the magnet and the coil corresponding to the maximum value of $V_{emf}$ was 1.57 mm. Therefore, the initial distance between the magnet and the coil in the practical device should be larger than 1.57 mm in order to obtain the maximum value of $V_{emf}$ generated in the coil. Figure 3c shows that the absolute value of

$V_{emf}$ versus the displacement of the magnet when the amplitude of the magnet is fixed. The curve shape is very similar with that in Figure 3b. The maximum value of $V_{emf}$ is independent of the amplitude of the magnet ($A_m$). Meanwhile, the magnet's position corresponding to the maximum value of $V_{emf}$ was 1.57 mm, also independent of $A_m$. As a result, the magnet's position corresponding to the maximum value of $V_{emf}$ is not related to the acceleration and the amplitude as shown in Figure 3b,c. Based on Figure 3b,c, the maximum value of $V_{emf}$ versus the maximum velocity of the magnet under different amplitudes of the magnet was obtained and shown in Figure 3d. It is clear that the maximum value of $V_{emf}$ is linear with the maximum velocity of the magnet when $A_m$ is fixed. Moreover, the slope of the curve depends on $A_m$. For a given coil–magnet structure, the distance between the magnet and the coil is known and so $A_m$ is fixed. Therefore, the maximum value of $V_{emf}$ in an EMG can be used to detect the maximum velocity of the magnet.

## 2.4. Theoretical Analysis of TENG

For a vertical contact-separation mode TENG as shown in Figure 1a, the electrons are injected from the Cu layer into the PTFE film, which leaves net positive charges in Cu layer and net negative charges on the surface of the PTFE film, when the

ADVANCED
SCIENCE NEWS
www.advancedsciencenews.com

ADVANCED
FUNCTIONAL
MATERIALS
www.afm-journal.de

Cu layer and PTFE film are brought into contact by an external force/pressure. When the external force is withdrawn, the Cu layer and the PTFE film separates and the $V_{oc}$ of the TENG increases linearly with the vertical gap distance ($d$) between the two triboelectric layers as given in the following equation[33]

$$V_{oc} = \frac{\sigma \cdot d}{\varepsilon_0} \tag{5}$$

where $\varepsilon_0$ is the permittivity in vacuum and $\sigma$ is the triboelectric charge density. Therefore, the $V_{oc}$ of the TENG reaches its maximum value when the vertical gap distance is equal to the original gap distance ($d_0$) and the maximum is

$$V_{oc,0} = \frac{\sigma \cdot d_0}{\varepsilon_0} \tag{6}$$

If the PDMS structure is considered as a spring structure, the following equation can be obtained by using the Hooker's law

$$F = k \cdot x = k \cdot (d_0 - d) \tag{7}$$

where $F$ is the external force, $x$ is the displacement of the top triboelectric material, and $k$ is the spring constant of the PDMS structure.

By combining Equations (5), (6), and (7), the following equation can be obtained

$$F = k \cdot d_0 \cdot \frac{V_{oc,0} - V_{oc}}{V_{oc,0}} \tag{8}$$

Hence, there is a linear relationship between the external force ($F$) and the relative variation of the $V_{oc}$. Thus, the relative variation of the open-circuit voltage of the TENG is a reliable parameter for measuring the magnitude of the external force/pressure applied onto the device.

On the other hand, according to Ampere's circuital law with Maxwell's addition, the displacement current ($J_D$) in the dielectrics with the presence of the surface-polarized charges can be defined as

$$J_D = \frac{\partial D}{\partial t} = \varepsilon \frac{\partial E}{\partial t} + \frac{\partial P_s}{\partial t} \tag{9}$$

where the displacement field $D$, the electric field $E$, and the polarization field $P_s$ are caused by surface-polarized charges. For a four-layer contact-separation mode TENG with two dielectrics with permittivity $\varepsilon_1$ and $\varepsilon_2$ and thicknesses $d_1$ and $d_2$, respectively, the corresponding displacement current density inside the TENG can be derived as[30]

$$J_D = \frac{\partial D_z}{\partial t} = \sigma_c \cdot \frac{dz}{dt} \cdot \frac{\frac{d_1 \varepsilon_0}{\varepsilon_1} + \frac{d_2 \varepsilon_0}{\varepsilon_2}}{\left( \frac{d_1 \varepsilon_0}{\varepsilon_1} + \frac{d_2 \varepsilon_0}{\varepsilon_2} + z \right)^2} \tag{10}$$

where $z$ is the gap distance and $\sigma_c$ is the surface charge density. Under short-circuit condition, the short-circuit current density

($J_{sc}$) in external circuit is equal to the displacement current density inside the TENG, namely
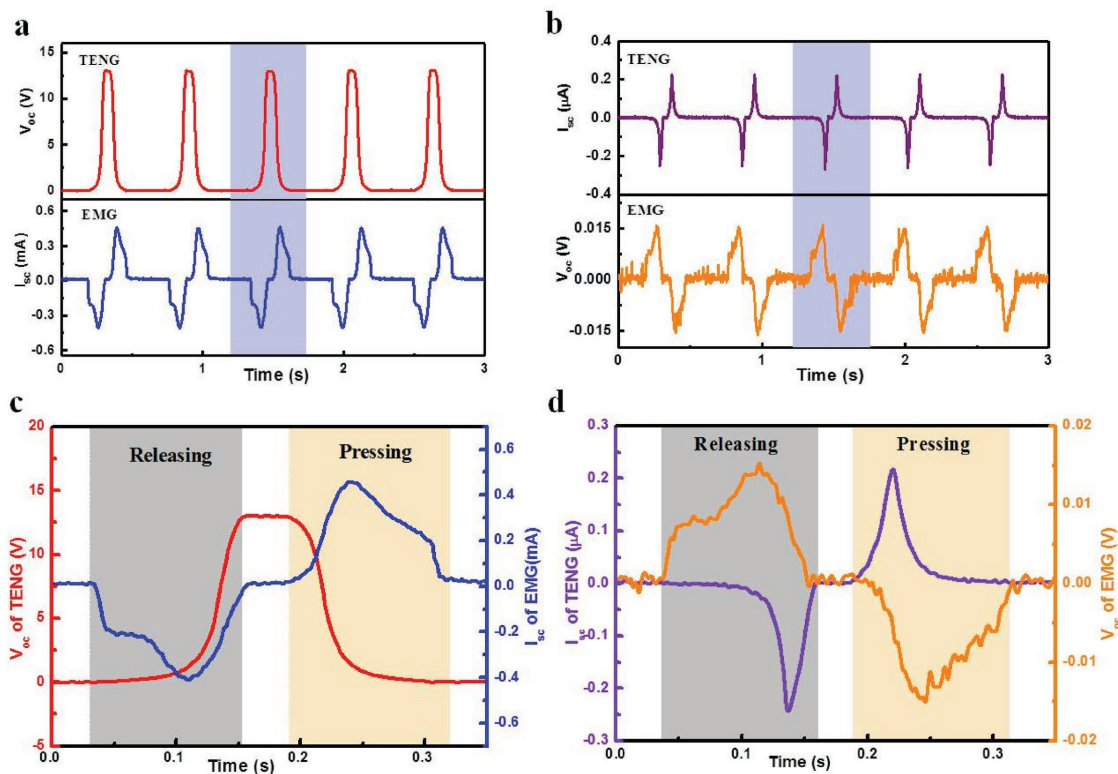
$$J_{sc} = J_D \tag{11}$$

Equations (10) and (11) mean that the value of $J_{sc}$ is proportional to the surface charge density and the speed at which the two dielectrics are being separated or contacted.

## 2.5. Output Characterization

The output signals of the hybridized sensor were collected when a 1.7 Hz periodic external force was applied on the device by a linear motor. Since TENG and EMG are independent, their output signals can be obtained separately and simultaneously as shown in **Figure 4**a,b. The open-circuit voltage ($V_{oc}$) and short-circuit current ($I_{sc}$) of the TENG could reach 13.1 V and 0.25 μA, respectively; while the $V_{oc}$ and the $I_{sc}$ of the EMG could reach 0.016 V and 0.45 mA, respectively, as indicated in Figure 4a,b. Therefore, the TENG has relatively high voltage and low current. On the contrary, the EMG has relatively high current but low voltage. The amplified voltage and current signals of the TENG and EMG are in Figure 4c,d. As displayed in Figure 4c, the $V_{oc}$ keeps increasing until reaching the maximum value when the PDMS structure returned its original condition. Then the $V_{oc}$ of the TENG kept constant until the external force is applied onto the TENG. Then the $V_{oc}$ of the TENG decreased to zero when the two triboelectric materials contact with each other. It indicates that the magnitude of the voltage can reflects the degree of contact between the two surfaces. Moreover, the response time of the developed sensor can be calculated from the process of applying the force and it is about 0.05 s. It is sufficient to collect the typing information of human beings since the average time difference typing is large than 0.1 s.

On the other hand, Figure 4c shows that the $I_{sc}$ of the EMG increased significantly from 0 mA at the beginning of the movement of the magnet. Subsequently the $I_{sc}$ gradually increased to its maximum value and then decreased to zero until the magnet stopped moving. Therefore, the $I_{sc}$ of the EMG always changes during the whole process of the magnet's movement, which indicates that the current signal of the EMG is a long-range effect. So the $I_{sc}$ of the EMG can reflect the dynamics of the magnet. The $V_{oc}$ of the EMG also has similar feature with the $I_{sc}$ as shown in Figure 4d, since the $V_{oc}$ is linear with the $I_{sc}$ as shown by Equation (4). Moreover, it can be derived from Equations (3) and (4) that the $V_{oc}$ and the $I_{sc}$ of the EMG are in relationship with the velocity of the magnet. Therefore, the output signals of the EMG are dynamic parameters that can be used to monitor the motion behavior of the magnet, which could be confirmed by the following experimental results.

Based on above analysis, it is clear that the voltage signal of the TENG part is very stable and is three orders (0–14 V) of magnitude greater than that of the EMG (0–0.015 V), which could decrease the demand of a sophisticated test equipment and allow for a lower measurement deviation. On the other hand, the current and voltage of the EMG part can reflect the movement characteristics of the object, but the current signal is much more stable than the voltage signal. Meanwhile, the
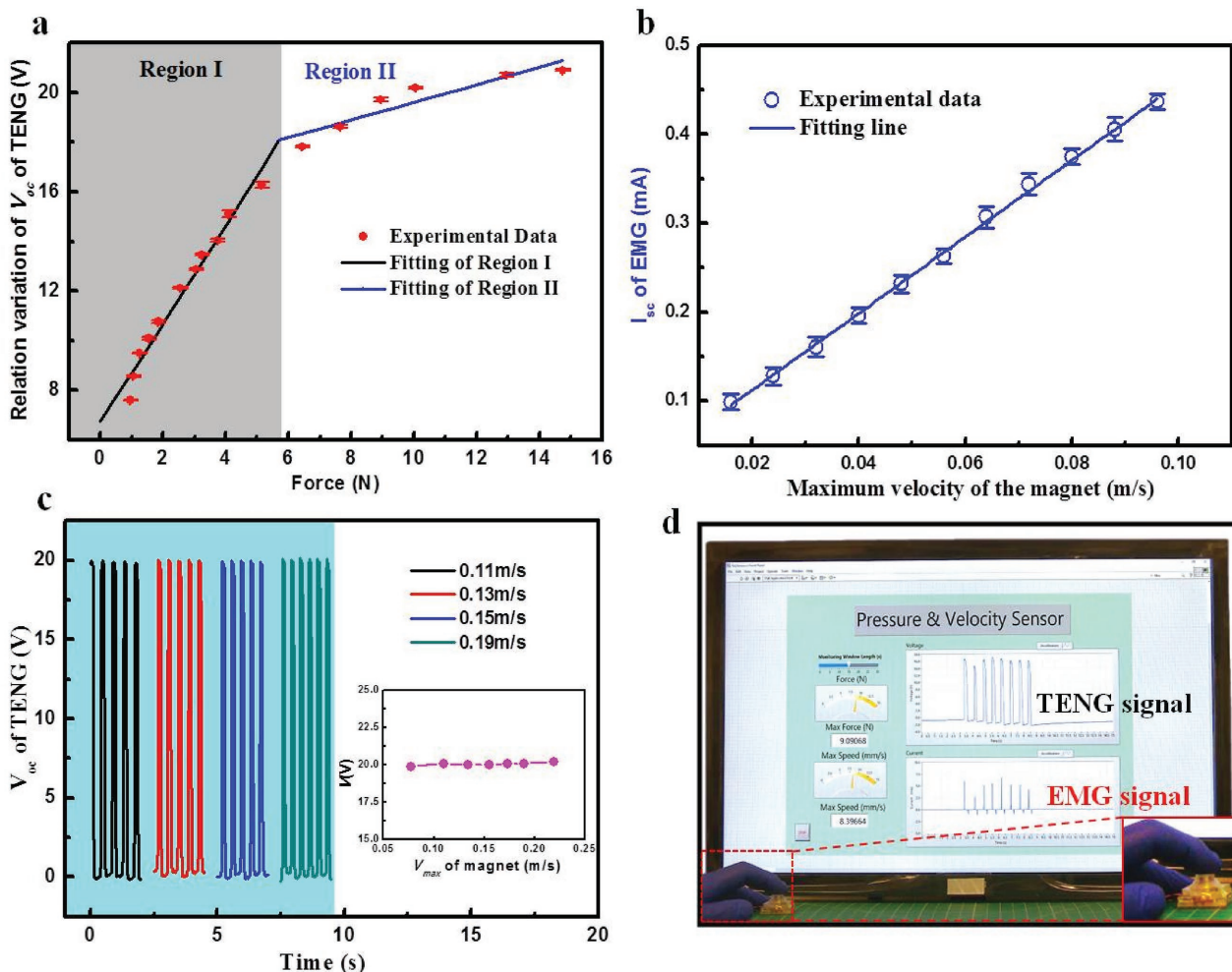
**Figure 4.** The open-circuit voltage and short-circuit current of EMG and TENG. a) Open-circuit voltage of TENG and short-circuit current of EMG measured simultaneously. b) Open-circuit voltage of EMG and short-circuit current of TENG measured simultaneously. c) The enlarged part in (a). d) The enlarged part in (b).

current of the EMG part (0–0.5 mA) is three orders of magnitude greater than that of the TENG part (0–0.25 μA). As a result, only the voltage signal of the TENG part and the current signal of the EMG part are measured systematically for the detection of multiple mechanical signals in the following experiments.

After the above analysis, the electrical output performance of the complementary EMG-TENG active sensor were systematically measured under different external conditions and the results were given in **Figure 5**, and Figures S5 and S6 (in the Supporting Information). A computer-controlled linear motor was used to supply a periodic force which could be detected by a force sensor. The real-time results of $V_{oc}$ and $I_{sc}$ of the TENG part under different external force are given in Figure S5a,b in the Supporting Information and the summarized relationship between $V_{oc}$ and $I_{sc}$ and the force are plotted in Figure 5a and Figure S5c (Supporting Information). During the process of processing data, the reference level of voltage was selected in the way that the $V_{oc}$ approached zero with the maximum force when the two triboelectric materials contact with each other tightly. It can be seen clearly from Figure 5a that the voltage curve can be divided into two regions based on different sensitivity. The sensitivity in region I was 2.01 V N$^{-1}$, much higher than that of 0.35 V N$^{-1}$ in region II. In Region I, the increase of the force results in the great change of gap distance ($d$) and then results in great relative variation of $V_{oc}$ as estimated in Equation (8). After the two triboelectric materials contact with each other, the increase of force only can make the PDMS layer deform and increase the effective contact area. Since the increase of contact

area is limited, the increase of the relative variation of $V_{oc}$ of TENG is slow and trends to saturate with the increase of the external force, as shown in Region II in Figure 5a.[34,35] To verify the feature that the $V_{oc}$ only depends on the magnitude of the external force rather than the loading velocity, the $V_{oc}$ response of the TENG was further measured under a constant force but different maximum velocity of loading. As revealed in Figure 5c, the $V_{oc}$ of the TENG almost unchanged as the maximal velocity increased from 0.08 to 0.23 m s$^{-1}$. Therefore, the $V_{oc}$ of the TENG is independent of the maximal velocity of the magnet. During the increase of the maximal velocity of the magnet, the frequency of the loading increases too and it increases from 2.3 to 2.9 Hz. Therefore, Figure 5c also shows that the open circuit voltage of TENG is independent of the frequency of the loading and unloading.

The real-time measurement result of $V_{oc}$ and $I_{sc}$ of the EMG part under different maximum velocity of the magnet are given in Figure S6a,b (Supporting Information), with the summarized relationship between $V_{oc}$ and $I_{sc}$ and the maximum velocity of the magnet plotted in Figure 5b and Figure S6c (Supporting Information). As shown in Figure 5b, the output current of the EMG increased with the maximal velocity of the magnet linearly. This result is in good agreement with the theoretical calculation. The sensitivity of the output current of the EMG part was calculated to be 4.3 mA (m s$^{-1}$)$^{-1}$. To demonstrate the stability of the ETAS further, a continuous force with a frequency of 2 Hz was applied onto the device. As shown in Figures S5d and S6d (Supporting Information), both the $V_{oc}$ of

**Figure 5.** Electrical output performance of the EMG-TENG active sensor. a) The relative variation of the $V_{oc}$ of the TENG part versus different external forces applied on the TENG. b) The short-circuit current of the EMG part versus the maximum velocity of the magnet. c) The open-circuit voltage of TENG versus time under different maximal velocity of magnet and same external force. The inset shows the relationship between the open-circuit voltage and the maximal velocity of magnet. d) Demonstration of the ETAS for recording the press force and velocity from keystroke.

the TENG part and the $I_{sc}$ of the EMG part were almost constant after more than 20 000 loading–unloading cycles. It illustrates that the hybridized sensor based on PDMS structure has excellent mechanical robustness and stability.

Based on the working principle of the ETAS, we demonstrated its capability of capturing the keystroke dynamics when the ETAS is pressed by a finger. The interface for acquiring the output signals of the ETAS and displaying the analysis results is shown in Figure 5d. During the process of pressing the ETAS, the voltage signals of the TENG part, and the current signals of the EMG part were recorded in real time by a data acquisition system. Then the maximum force and maximum velocity applied onto the ETAS were calculated by using the respective sensitivity of the TENG part and the EMG part. As can be seen from Figure 5c and Video S1 (Supporting Information), the TENG voltage signal and EMG current signal can be acquired simultaneously. Moreover, the maximum force and maximum velocity can be displayed, too. In addition, the TENG part in the ETAS can also be used as an energy harvester to scavenge the biomechanical energy. As shown in Figure S7 and Video S2 (Supporting Information), the

letter "TENG" assembled by 30 blue light emitting diodes (LEDs) connected in series can be lighted up directly by the TENG part, when a finger pressed on the device.

According to the above experimental analysis, the integrated and hybridized ETAS demonstrated in this work can not only detect multiple mechanical triggering signals (such as force/pressure, velocity) at the same time, but also capture the mechanical energy from the impact or press and then convert into electrical energy. Therefore, the ETAS has a huge potential application in the human–machine interface, identification, intelligent security systems, energy harvesting, and other fields. For example, the device may be integrated into the keyboard as an identification method for user's access to the computer system. As we know, each person's typing habits will be different due to the individual differences between people. The typing habit includes typing force, key rate, typing frequency, and even force direction. Therefore, if this fabricated hybridized sensor is integrated into the keyboard, it can collect the signals of the force, velocity, and frequency of typing from the user and then the personal identification is realized. Compared to

a technique that has only one identification function, this work can provide simultaneous identification of two or even three signals and thus have higher security. In addition, the ETAS can also collect the useless kinetic energy generated during the typing process and converts it into electrical energy. The energy can be used to trigger the alarm of the intrusion system. On the other hand, it can be stored in capacitors to power other microelectronic devices.

## 3. Conclusion

In summary, we demonstrated a flexible and integrated electromagnetic-triboelectric active sensor for detecting multiple mechanical triggering signals simultaneously. The combination of an EMG and a TENG was able to achieve a good complement of their respective advantages. The output voltage of TENG part could be used to detect force/pressure signals and the experimental results showed that its sensitivity was about $2.01$ V N$^{-1}$. The theoretical calculation indicated that the output current of EMG was linearly related to the maximum velocity of the mechanical triggering, which was proved by the measurement. Moreover, the experimental results showed that the sensitivity of EMG part was about $4.3$ mA (m s$^{-1}$)$^{-1}$. The robustness and stability of this hybridized sensor were also validated after more than 20 000 cycles of force loading–unloading experiments. The demonstration indicates that this hybridized sensor not only can record the typing behavior of the finger precisely but also harvest the unused mechanical energy from typing and convert into electrical energy for powering other electronic devices. This work may open up a new beginning to the fundamental understanding of the hybridized electromagnetic-triboelectric active sensor. Moreover, it can provoke a new research field for application of electromagnetic-triboelectric active sensors in touch sensing, personal identification, and even security system.

## 4. Experimental Section

*Fabrication of the Hybridized EMG-TENG Active Sensor*: This hybridized sensor mainly consists of up PDMS part and bottom coil part. For up part, a PMDS button structure was fabricated first and its detailed fabrication process was depicted in Figure S1 (Supporting information). Then a 40 µm Cu foil was attached to the inside of the PDMS button structure as the top electrode and the triboelectric material. Meanwhile, one lead wire was connected to the top Cu electrode for electrical measurement. For bottom part, a Cu coil with turns of 600 was fixed on the center of an acrylic sheet with dimension of $25 \times 25 \times 1.6$ mm$^3$ prepared by laser cutting at first. The height, the inner and out diameters of the coil were 2.4, 4, and 11 mm, respectively. Then a circular Cu foil was attached onto the coil's surface as the bottom electrode and another lead wire was connected to this foil for electrical measurement. Subsequently, a layer of 200 µm polytetrafluoroethylene (PTFE) film, as another triboelectric material, was attached onto the bottom electrode. The area of the bottom Cu electrode and the PTFE film are same with that of the coil. At last, the up PDMS part, the bottom coil part and another piece of acrylic sheet ($25 \times 25 \times 1.6$ mm$^3$) are assembled into a hybridized sensor by using Kapton tape. The initial distance between the top Cu electrode and bottom PTFE film is about 5 mm. During this fabrication process of the PDMS strucuture, the elastomer base, and the elastomer curing agent are mixed with a mass ratio of 10:1 (Sylgard 184 silicone elastomer kit manufactured by Dow Corning corporation). After pouring the mixed solution into the mold, they were kept in a convection oven at 60 °C for 6 h until the PDMS got cured. After fabrication of the PDMS structure, the relationship between the external force applied on the top surface and the displacement of the top surface are measured and the result is shown in Figure S8 (Supporting Information). From Figure S8 (Supporting Information), the spring constant of the PDMS structure can be calculated and is about 2.8 N mm$^{-1}$.

*Measurement of the Devices*: A linear motor (LinMot E1100) was used to provide periodic mechanical motion for the ETAS. The force applied on the ETAS was measured by a dual-range force sensor (Vernier Software & Technology, DFS-BTA). The electrical outputs of the ETAS were measured by an electrometer (Keithley, 6514) and analyzed through a software platform based on LABVIEW program. In our experiment, we set the lowest value of the $V_{oc}$ of TENG as zero in every continuous measurement. Therefore, the $V_{oc}$ of TENG is always positive which has a zero baseline. The relative variation of the $V_{oc}$ is equal to the maximum value of $V_{oc}$ of TENG.

## Supporting Information

Supporting Information is available from the Wiley Online Library or from the author.

## Conflict of Interest

The authors declare no conflict of interest.

[1] I. Khan, F. Belqasmi, R. Glitho, N. Crespi, M. Morrow, P. Polakos, *IEEE Commun. Surv. Tutor.* **2016**, *18*, 553.
[2] M. T. Lazarescu, L. Lavagno, *Handbook of Hardware/Software Codesign*, (Eds.: S. Ha, J. Teich), Springer, Netherlands **2017**, p. 1.
[3] F. Wang, L. Hu, J. Hu, J. Zhou, K. Zhao, *IETE Tech. Rev.* **2017**, *34*, 122.
[4] A. Nag, S. C. Mukhopadhyay, J. Kosel, *IEEE Sens. J.* **2017**, *17*, 3949.
[5] F.-R. Fan, Z.-Q. Tian, Z. L. Wang, *Nano Energy* **2012**, *1*, 328.
[6] Z. L. Wang, *ACS Nano* **2013**, *7*, 9533.
[7] Z. L. Wang, J. Chen, L. Lin, *Energy Environ. Sci.* **2015**, *8*, 2250.
[8] J. Chen, Y. Huang, N. Zhang, H. Zou, R. Liu, C. Tao, X. Fan, Z. L. Wang, *Nat. Energy* **2016**, *1*, 16138.
[9] A. Li, Y. Zi, H. Guo, Z. L. Wang, F. M. Fernández, *Nat. Nanotechnol.* **2017**, *12*, 481.

**ADVANCED
SCIENCE NEWS**
www.advancedsciencenews.com

**ADVANCED
FUNCTIONAL
MATERIALS**
www.afm-journal.de

[10] C. Wu, R. Liu, J. Wang, Y. Zi, L. Lin, Z. L. Wang, *Nano Energy* **2017**, *32*, 287.

[11] J. W. Lee, H. J. Cho, J. Chun, K. N. Kim, S. Kim, C. W. Ahn, I. W. Kim, J.-Y. Kim, S.-W. Kim, C. Yang, J. M. Baik, *Sci. Adv.* **2017**, *3*, e1602902.

[12] K. Y. Lee, H. J. Yoon, T. Jiang, X. Wen, W. Seung, S. W. Kim, Z. L. Wang, *Adv. Energy Mater.* **2016**, *6*, 1502566.

[13] Y. C. Lai, J. Deng, S. Niu, W. Peng, C. Wu, R. Liu, Z. Wen, Z. L. Wang, *Adv. Mater.* **2016**, *28*, 10024.

[14] H. Peng, X. Fang, S. Ranaei, Z. Wen, A. L. Porter, *Nano Energy* **2017**, *35*, 358.

[15] S. L. Zhang, Y. C. Lai, X. He, R. Liu, Y. Zi, Z. L. Wang, *Adv. Funct. Mater.* **2017**, *27*, 1606695.

[16] W. Li, D. Torres, R. Díaz, Z. Wang, C. Wu, C. Wang, Z. Lin Wang, N. Sepúlveda, *Nat. Commun.* **2017**, *8*, 15310.

[17] X. Chen, Y. Song, Z. Su, H. Chen, X. Cheng, J. Zhang, M. Han, H. Zhang, *Nano Energy* **2017**, *38*, 43.

[18] M. Shi, H. Wu, J. Zhang, M. Han, B. Meng, H. Zhang, *Nano Energy* **2017**, *32*, 479.

[19] H. Yu, X. He, W. Ding, Y. Hu, D. Yang, S. Lu, C. Wu, H. Zou, R. Liu, C. Lu, Z. L. Wang, *Adv. Energy Mater.* **2017**, *7*, 1700565.

[20] P. Wang, K. Tanaka, S. Sugiyama, X. Dai, X. Zhao, J. Liu, *Microsyst. Technol.* **2009**, *15*, 941.

[21] M. A. Halim, H. Cho, M. Salauddin, J. Y. Park, *Sens. Actuator, A* **2016**, *249*, 23.

[22] Y. Zi, H. Guo, Z. Wen, M.-H. Yeh, C. Hu, Z. L. Wang, *ACS Nano* **2016**, *10*, 4797.

[23] X. Ren, H. Fan, C. Wang, J. Ma, S. Lei, Y. Zhao, H. Li, N. Zhao, *Nano Energy* **2017**, *35*, 233.

[24] U. Khan, S.-W. Kim, *ACS Nano* **2016**, *10*, 6429.

[25] Z. Wen, H. Guo, Y. Zi, M.-H. Yeh, X. Wang, J. Deng, J. Wang, S. Li, C. Hu, L. Zhu, *ACS Nano* **2016**, *10*, 6526.

[26] Y. Hu, J. Yang, S. Niu, W. Wu, Z. L. Wang, *ACS Nano* **2014**, *8*, 7442.

[27] Z. L. Wang, T. Jiang, L. Xu, *Nano Energy* **2017**, *39*, 9.

[28] Y. Xi, H. Guo, Y. Zi, X. Li, J. Wang, J. Deng, S. Li, C. Hu, X. Cao, Z. L. Wang, *Adv. Energy Mater.* **2017**, *7*, 1602397.

[29] S. Li, W. Peng, J. Wang, L. Lin, Y. Zi, G. Zhang, Z. L. Wang, *ACS Nano* **2016**, *10*, 7973.

[30] Z. L. Wang, *Mater. Today* **2017**, *20*, 74.

[31] C. Zhang, W. Tang, C. Han, F. Fan, Z. L. Wang, *Adv. Mater.* **2014**, *26*, 3580.

[32] J. Camacho, V. Sosa, *Rev. Mex. Fís. E* **2013**, *59*, 8.

[33] L. Lin, Y. Xie, S. Wang, W. Wu, S. Niu, X. Wen, Z. L. Wang, *ACS Nano* **2013**, *7*, 8266.

[34] J. Luo, F. R. Fan, T. Zhou, W. Tang, F. Xue, Z. L. Wang, *Extreme Mech. Lett.* **2015**, *2*, 28.

[35] G. Zhu, W. Q. Yang, T. Zhang, Q. Jing, J. Chen, Y. S. Zhou, P. Bai, Z. L. Wang, *Nano Lett.* **2014**, *14*, 3208.